crystals

MDPI

Article

Growth, Structure, and Electrical Properties of $AgNbO_3$ Antiferroelectric Single Crystal

Dengxiaojiang Zhao, Zhenpei Chen, Borui Li, Shi Feng and Nengneng Luo *

State Key Laboratory of Featured Metal Materials and Life-Cycle Safety for Composite Structures, School of Resources, Environment and Materials, Guangxi University, Nanning 530004, China; zhaodengxiaojiang@gmail.com (D.Z.); czp341114@163.com (Z.C.); lbr_lzj@hotmail.com (B.L.); fs18226818818@163.com (S.F.)

* Correspondence: nnluo@gxu.edu.cn

Abstract: $AgNbO_3$ (AN) lead-free antiferroelectric material has attracted great attention in recent years. However, little focus has been directed toward a single crystal that can provide more basic information. In this study, we successfully grew high-quality AN single crystals, using a flux method, with dimensions of $5 \times 5 \times 3$ mm^3. A systematic investigation into the crystal structure, domain structure, and electrical properties of a [001]-oriented AN single crystal was conducted. X-ray diffraction and domain structure analysis revealed an orthorhombic phase structure at room temperature. Stripe-like 90° domains aligning parallel to the [110] direction with a thickness of approximately 10–20 μm were observed using a polarized light microscope. The temperature dependence of dielectric permittivity showed M1-M2, M2-M3, and M3-O phase transitions along with increasing temperature, but the phase transition temperatures were slightly higher than those of ceramic. The AN single crystal also exhibited double polarization-electric field (*P*-*E*) hysteresis loops, which enabled good recoverable energy-storage density and efficiency comparable to ceramic. Additionally, double *P*-*E* loops were kept stable at various temperatures and frequencies, demonstrating robust stability and confirming typical antiferroelectric characteristics. Our work provides valuable insights into understanding the fundamental antiferroelectric properties of AN-based materials.

Keywords: $AgNbO_3$; single crystal; antiferroelectric; domain

check for updates

Citation: Zhao, D.; Chen, Z.; Li, B.; Feng, S.; Luo, N. Growth, Structure, and Electrical Properties of $AgNbO_3$ Antiferroelectric Single Crystal. *Crystals* **2024**, *14*, 235. https://doi.org/10.3390/cryst14030235

Academic Editors: Bhargav Akkinepally and Mengjie Chen

Received: 11 January 2024
Revised: 17 February 2024
Accepted: 27 February 2024
Published: 28 February 2024

Copyright: © 2024 by the authors. Licensee MDPI, Basel, Switzerland. This article is an open access article distributed under the terms and conditions of the Creative Commons Attribution (CC BY) license (https://creativecommons.org/licenses/by/4.0/).

1. Introduction

Antiferroelectric (AFE) materials are distinct from ferroelectric (FE) materials due to antiparallel polarization orientations in adjacent crystal unit cells, resulting in a macroscopic absence of spontaneous polarization [1]. Once external stimulations are applied, such as temperature, electric field, or mechanical stress, they usually undergo AFE-to-ferroelectric (FE) reversible phase transitions and thus exhibit properties linked to the high electric field-induced polarization [2]. Due to the big differences between the initial AFE state and the electric field-induced FE state, AFE materials exhibit great potential in the application of high-energy-storage capacitors; they also make excellent electrocaloric solid-cooling units and good thermal conductivity switching devices [3]. Particularly, AFE materials have higher energy-storage capabilities and are attracting growing attention because of the demand for miniaturization and integration. Generally, a higher maximum polarization (P_{max}) and breakdown electric field (E_b), along with a lower remnant polarization (P_r), are good for achieving higher recoverable energy-storage density (W_{rec}) in a dielectric material [4,5]. Due to the environmental and health toxicity of lead and lea oxide-containing compounds, lead-free AFE materials have garnered worldwide research interest in the context of sustainable development; $NaNbO_3$ (NN)- and $AgNbO_3$ (AN)-based material systems are among such materials of interest [6].

The AN stands out with Its relatively high saturation polarization strength (~50 μC/cm²) and rich structural phase transitions [7]. It undergoes a series of phase transitions before the

paraelectric phase with an increase in temperature, including the M1 orthorhombic phase ($Pmc2_1$), and M2 and M3 orthorhombic phases (*Pbcm*) [8,9]. The M1 is generally considered to be a ferroelectric (FE) phase, while the M2 and M3 are disordered AFE phases with different displacement disorder sites in the B-sites [10,11]. The AN ceramics generally exhibit a good W_{rec} of 2 J/cm^3 [12]. However, due to the low-temperature FE M1 phase, high remnant polarization with large hysteresis always exists, which results in limited energy-storage density and low efficiency. Therefore, intensive investigations have focused on increasing the stability of the AFE phase to optimize energy-storage performance. They usually rely on methods of optimizing the parameters through ceramics and thin films, such as chemical modification and structural design [13–15]. So far, significant breakthroughs have been achieved in recent years and outstanding W_{rec} of 13.13 J/cm^3 with a high η of 56% was achieved in AN-based thin film by employing oxygen ion surface plasma technology in conjunction with the sol-gel method [14]. Despite the great progress, however, the obtained AN-based materials are mostly ceramics or thin film, in which the microstructure is inhomogeneous, restricting the further improvement of energy-storage density [16]. Furthermore, as ceramic and thin film materials are polycrystalline, the influence of other factors such as grain boundaries and grain size must be taken into account, which creates obstacles to the understanding of the intrinsic performance and mechanisms among them [17]. Therefore, it is of great importance to pay attention to the crystal structure and the intrinsic performance through fundamental research, which may create new opportunities for the further development of AN.

It is well known that, in the study of intrinsic structures and inherent properties, a single crystal is undoubtedly a more ideal research subject compared with ceramic or film. Oriented single crystals can offer more information and exhibit superior performance, most of which is intricately linked to their unique AFE domain structure [18,19]. However, due to the significant challenge of growing AFE single crystals, there are limited reports on the domain structure and electrical properties of the AN single crystal. Even in the limited references, investigations on the structure and electrical properties are discrete, and we are lacking a comprehensive study on them. Therefore, it is of significant importance to grow high-quality AN single crystals and to conduct a combination investigation on both the structure and electrical properties.

The basic properties of AN single crystals are challenging to obtain due to vacancy defects caused by the absence of Ag^+, which is easily reduced and transformed into metallic Ag at high temperatures even below its melting point. The oxygen atoms will form oxygen molecules to maintain charge neutrality, resulting in the production of oxygen [10]. Therefore, it can ensure the quality of AN single crystals if the volatilization of Ag can be controlled to a certain extent, allowing it to enter the crystal lattice during the growth process of AN single crystals. In this work, a flux method was employed for the growth of AN single crystals in an oxygen atmosphere. The inclusion of AgCl as a flux decreases the sintering temperature of crystal nucleation to minimize Ag volatilization; furthermore, the Ag^+ in AgCl partially compensates for the lost Ag due to Ag vaporization in the melt. High-quality AN single crystals with a geometrically regular shape and dimensions of 5 × 5 × 3 mm^3 were successfully grown. The phase structure, domain structure, temperature-dependent phase transitions, and electrical properties along [001] orientation were systematically investigated. The temperature and frequency stability of the energy-storage performance were also studied. Our work could provide a more fundamental understanding of lead-free AFE from the aspect of single crystals.

2. Experimental Procedures

2.1. Fabrication

In this study, a modified co-solvent method was utilized to grow the AN single crystal. Firstly, the raw powder was prepared by a solid-solution synthesis method. The raw powders of Ag_2O (99.7%) (Sinopharm Chemical Reagent Co., Ltd., Shanghai, China) and Nb_2O_5 (99.5%) (Jiujiang Tanbre Co., Ltd., Shanghai, China) were weighed according to the

stoichiometric ratio. Then, ball-milling was conducted for 8–10 h using zirconia balls as the grinding medium and anhydrous ethanol as the mixing medium. Thereafter, the mixtures were dried in a hot chamber for 4–6 h. After being ball-milled and dried, the obtained mixtures were calcined at 900 °C for 6 h under an oxygen atmosphere to obtain a pure phase and restrict the loss of silver. Thereafter, the AN calcined powder was mixed with a certain amount of AgCl (99.5%) (Sinopharm Chemical Reagent Co., Ltd., Shanghai, China), which was put into a double corundum crucible. Finally, the crucible was put in a furnace and heated to ~1180 °C for several hours in an oxygen atmosphere to melt the mixture, followed by slowly cooling down for 8–20 h to ~1140 °C for nucleation, and cooled down to room temperature. The schematic flow-process diagram of the crystal growth process is illustrated in Figure 1a, where T1 is the nucleation temperature and T3 is the temperature at which the crystal particles begin to grow. Following this, the AN single crystal was treated with ammonia to remove residual AgCl accumulated during this process. Finally, the sample was polished and oriented by using X-ray diffraction (XRD).

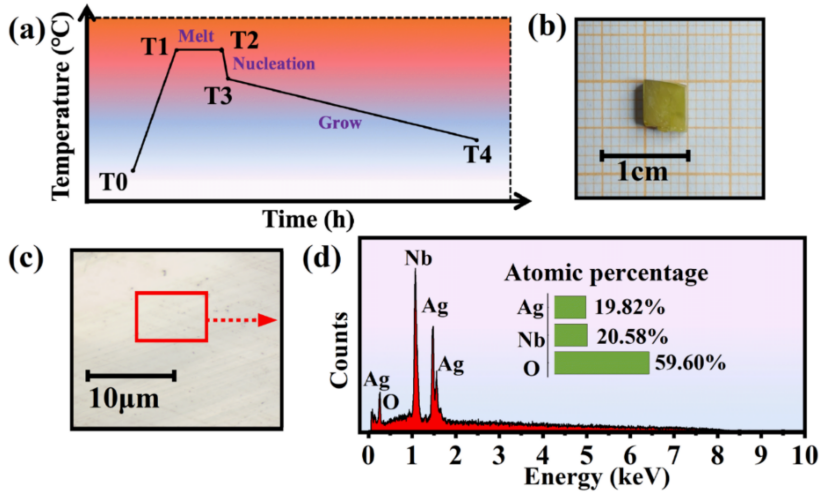


Figure 1. (**a**) The schematic flow-process diagram for AN single crystal growth. (**b**) A representative of the as-grown AN single crystal after being taken out from crucible. (**c**) The SEM morphology of AN single crystal and (**d**) the atomic percentage calculated from the EDS analysis mapped in the red boxed area of (**c**).

2.2. Characterization

XRD (SmartLab-3 kW, Rigaku Ltd., Tokyo, Japan) using Cu Kα radiation was performed on the ground AN powder and the naturally grown facet of the crystal to determine the crystal structure and confirm the (001) orientation. Before testing, the AN single crystal needs to be fully ground with alcohol as the grinding medium for half an hour. For AN single crystals oriented along the natural plane, it is necessary to use abrasive tools to grind them smoothly and carefully with sandpaper to ensure that the orientation will not deviate. The in situ high-temperature XRD measurements were conducted with a high-temperature control system chamber. The XRD patterns were collected at various temperatures in the 2θ range of 20–80° with step size of 0.02° using the Bragg–Brentano geometry. Each pattern collection took approximately 1 h and the ramping rate between different temperatures was 5 °C/min.

Scanning electron microscopy (SEM) (Pro X, Phenom, The Netherlands) and energy dispersive spectrum (EDS) were used to examine the surface morphology and the elemental composition ratio of the AN single crystal. The domain structure was observed using a PLM (Axioscope 5, Carl Zeiss AG, Oberkochen, Germany) in the transmission mode. Before that, the AN single-crystal sample was ground and polished to a thickness of approximately ~50 μm to ensure optimal transparency and achieve a mirror-like surface finish. Then, it was annealed at 600 °C for 1 h to eliminate the residual stress. The transmittance was determined using a Fourier Transform Infrared Spectrometer (FT-IR) (IRTracer-100,

Shimadzu Corporation, Kyoto, Japan) in the frequency range between 650 cm^{-1} and 4000 cm^{-1}.

Dielectric permittivity and loss as a function of temperature were measured by using a precision impedance analyzer (DMS2000, Balab, Wuhan, China) and connecting with a temperature-controlling system. The AN single crystal for the dielectric temperature spectrum was ground to a thickness of ~0.5 mm; the silver paste was painted on both surfaces and then sintered at ~600 °C for 30 min. The antiferroelectric properties were measured using a ferroelectric testing system (TF Analyzer 3000, AixACCT, Aachen, Germany). Before conducting electrical performance testing, the sample needs to be ground with high-grit sandpaper to about ~120 μm, and then sprayed with gold electrodes on both sides.

3. Results

Figure 1b shows the photo of the as-grown AN single crystal that was directly taken out of the flux in the crucible. The AN single crystal is yellow in color with a regular square shape. To assess the quality of the AN single crystal, the SEM morphology and EDS elemental analysis were conducted, as shown in Figure 1c,d. A dense and smooth surface without pores and defects is observed in the single crystal. The EDS analysis demonstrates that the atomic ratio of Ag:Nb:O is approximately 1:1:3, close to its nominal chemical composition. These results indicate that the as-grown AN single crystal is of high quality with minimal composition segregation.

Figure 2a shows the XRD patterns of AN calcined powder and single-crystal powder. All diffraction peaks are well indexed with the standard XRD pattern (PDF#70-4738), implying that both calcined powder and single-crystal powder of AN exhibit pure single-phase perovskite structure. To further determine the phase structure, Rietveld refinement was conducted on the AN single-crystal powder, as shown in Figure 2b. The XRD pattern is identified as a $Pmc2_1$ structural model, and the long axis c is approximately 3 times larger than a (where a and c are cubic perovskite cell parameters), which is consistent with its inherent AFE structure [20,21]. A schematic of the fitted crystal structure is shown in the inset of Figure 2b.

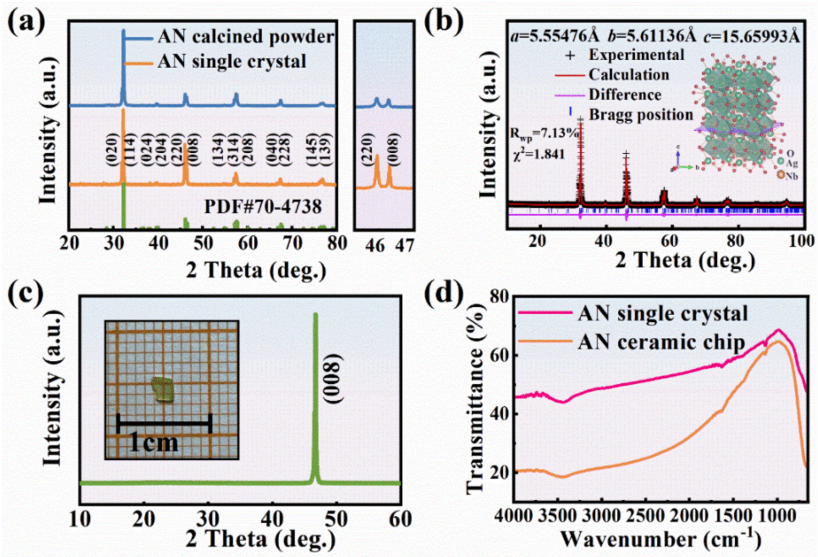


Figure 2. (**a**) XRD patterns of AN calcined powder and single-crystal powder after crushing. (**b**) Rietveld refinement results of AN single-crystal powder. (**c**) XRD pattern and photo for [001]-oriented AN single crystal. (**d**) FT-IR spectroscopy for [001]-oriented AN single crystal and ceramic chip.

After orienting and polishing along the [001] direction, a nearly transparent AN single crystal is observed, as shown in the inset of Figure 2c. The XRD pattern of the processed AN single crystal demonstrates only a strong (008) diffraction peak in Figure 2c,

indicating a good orientation along [001] direction. To evaluate the infrared transmittance of the [001]-oriented single crystal, FT-IR spectroscopy was conducted and is shown in Figure 2d. The AN single crystal possessed high transmittance over 60% around 1000 cm^{-1}, which exhibited a certain decrease with the increase of wavenumber. Additionally, strong absorption peaks on the rightmost side of the spectra are below 1000 cm^{-1} and no other major peaks beyond 1000 cm^{-1} are observed, which is mainly associated with the metal oxide bonds of niobium and silver [22,23]. Overall, the infrared transmittance of the [001]-oriented single crystal is higher than that of the AN ceramic [24,25]. This suggests that the AN single crystal involves fewer point defects, thereby enhancing the infrared light transmittance.

The domain microstructure is closely related to the microscopic symmetry of a FE/AFE single crystal. In theory, the symmetry of the crystal structure can be determined by analyzing the extinction phenomenon of the spontaneous polarization in the direction of projection on a particular crystal plane. Meanwhile, through observation from a specific face, the two-domain type structure is more likely to occur than patterns containing multiple domain variants, particularly for non-cubic sample geometry, due to the energy degeneracy of these domain states [26,27]. However, light microscopy images depicting such domain structures are rarely reported in AN single crystal. To investigate the domain structure, a PLM was applied on the [001]-oriented AN single crystal at RT. Figure 3a–f show the domain structure at 45° (P/A: 45°) and 0° (P/A: 0°) at various magnifications. The dipoles intersect along the [110] and [1$\bar{1}$0] directions, forming stripe-like 90° domains with width in the range of 10~20 μm. The narrow domain boundaries between domains with the same orientation are attributed to the reduced elastic energy generated by the strain near the walls. It is worth noting that a significant extinction of domains is found at P/A: 0° in the [001]-oriented AN single crystal, as shown in Figure 3b, which further confirms the orthorhombic structure.

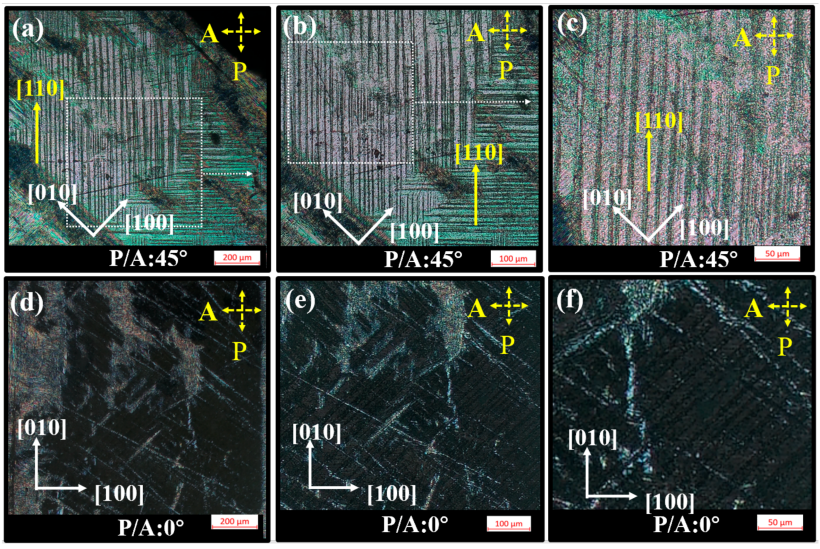


Figure 3. Domain structure observed by polarized light microscope at 45° (P/A: 45°) and 0° (P/A: 0°) for [001]-oriented AN single crystal at the magnifications of at (**a**,**d**)10×, (**b**,**e**) 20×, (**c**,**f**) 50×.

Figure 4a shows the temperature dependence of dielectric permittivity (ε_r) and loss (tanδ) for the [001]-oriented AN single crystal from RT to 450 °C in various frequencies. Three distinct dielectric anomalies are observed, corresponding to three phase transitions of M1-M2, M2-M3, and M3-O that are similar to those generally observed in the ceramic components. This means that the crystallinity and orientation have little effect on the phase structure and its transition sequence. It should be noticed that the phase transition temperatures of M1-M2, M2-M3, and M3-O are 80 °C, 295 °C, and 420 °C, respectively, which are slightly higher than those of ceramic. It is interesting that the [001]-oriented single

crystal exhibits higher dielectric permittivity with lower dielectric losses in comparison with AN ceramic. This disparity may be attributed to the substantial anisotropy in the dipole orientation of the single crystal [10]. In addition, the lower number of defects, more ordered lattice, and no grain boundaries compared to ceramics may also contribute to the phenomenon above.

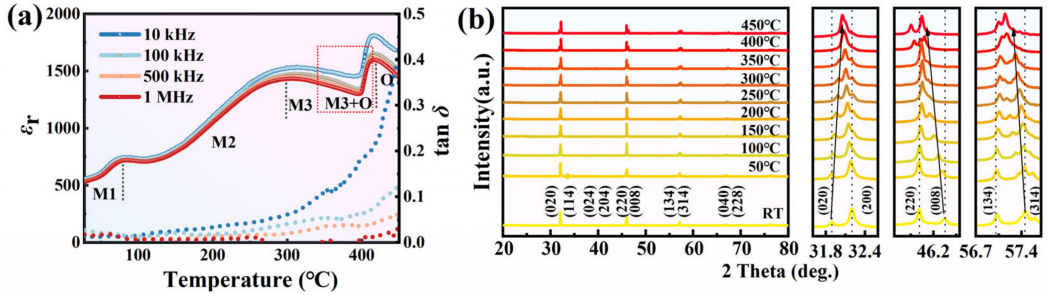


Figure 4. (**a**) Temperature dependence of dielectric permittivity and loss for [001]-oriented AN single crystal. (**b**) Temperature dependence of XRD patterns for AN single-crystal powder.

Temperature dependence XRD patterns were conducted to investigate the phase transition. The XRD patterns were indexed based on the standard cubic perovskite structure, as shown in Figure 4b. Consistent with previous findings, the AN exhibits a complex phase transition along with increasing temperature, although the M-phase shows minimal differences in the average XRD structure [10]. In the partially magnified diffraction curves, the arrows show the shift in position of the diffraction peaks with temperature. It is observed that the (020) peak shifts to a higher diffraction angle with increasing temperature, while the (008) and (314) peaks shift to a lower angle. Notably, the position of the (008) peak gradually shifts and merges with the (220) peak to form a single peak, and then splits into two peaks above 400 °C. These indicate the change of crystal parameters and increased symmetry with increasing temperature. The evolution of the AN phase structure can be better understood by applying Rietveld refinement to the XRD spectra. The as-refined lattice parameters are show in Table 1. The lattice parameters *a* and *b* get closer, while c increases continuously with increasing temperature, showing an increase in crystal symmetry. It is noteworthy that the phase transition is not abrupt but exhibits a gradual transition behavior. The phase transition process is consistent with the dielectric anomalies and indicates a slight increase in phase transition temperature than that of ceramic, which may be attributed to the combination of excellent single-crystal quality and anisotropies [21]. This also indicates that the phase transition in the AN single crystal is more difficult than that in AN ceramic. Therefore, a longer interval of M3-to-O phase process with a lengthy two-phase transition region is observed.

Table 1. The refining results and the unit cell parameters of AN.

T (°C)	Space Group	R_{wp} (%)	χ2	*a* (Å)	*b* (Å)	*c* (Å)
RT	$Pmc2_1$	7.13	1.841	5.55476	5.61136	15.65993
150	*Pbcm*	8.22	1.848	5.55789	5.604412	15.67906
300	*Pbcm*	9.19	1.915	5.56053	5.59716	15.72024
450	*Cmcm*	9.89	1.939	5.57109	5.59778	15.75651

Figure 5a–e present the *P-E* loops and *I-E* curves of the [001]-oriented AN single crystal at different electric fields. At low and medium electric fields, the *P-E* loops increase almost linearly with the increase of the electric field but exhibit a small maximum polarization. As the electric field increases beyond 150 kV/cm, the *P-E* loops broaden and gradually change from a linear type to double hysteresis loops, in which the polarization exhibits a remarkable increase with the electric field. The *I-E* curve accompanying this process shows the peaks related to the E_A and AFE–FE (E_F), indicating that the phase for [001]-oriented

AN single crystal has transformed from the antiferroelectric phase to the ferroelectric phase under the induction of the electric field. This transformation results in a significant improvement in the W_{rec} and η after inducing phase transition. At 200 kV/cm, a double *P-E* loop is observed with a high P_{max} of 42.2 μC/cm^2, giving a signature of AFE feature. It should be noted that P_r is ~11.3 μC/cm^2, which may be attributed to the weak ferroelectric property permeated in the AFE matrix [28]. At the same time, the *I-E* curve at 200 kV/cm exhibits four current peaks, further indicating its AFE nature. It can be ascertained from *I-E* curves that the phase transitions electric field E_F and E_A are located around ~151 kV/cm and ~59 kV/cm, respectively. It can be seen that the W_{rec} increases continuously and exhibits an obvious enhancement around the AFE-FE phase transition electric field, which finally reaches a maximum value of 1.34 J/cm^3 at 200 kV/cm. On the contrary, the η exhibits an opposite trend and reaches a maximum value of around 30%, due to the significantly increased remnant polarization and large hysteresis, which are similar to those observed in AN ceramic [16].

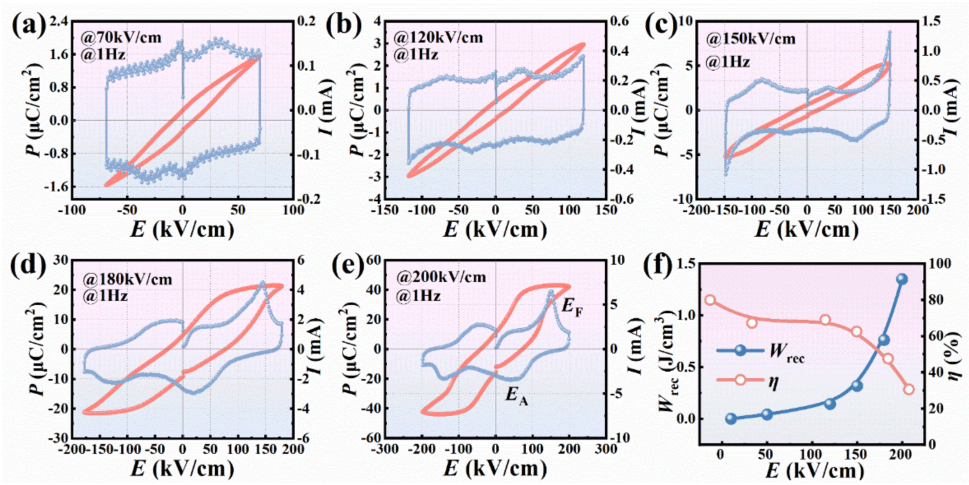


Figure 5. (**a**–**e**) Induce-electric dependence of *P-E* loops under 200 kV/cm for [001]-oriented AN single crystal at RT. (**f**) W_{rec} and η derived from the *P-E* loops in (**a**–**e**).

Figure 6a illustrates the temperature dependence of double *P-E* loops of the [001]-oriented AN single crystal measured from RT to 120°C at 200 kV/cm, in which typical double-like *P-E* loops can be observed in the whole temperatures. The value of P_r and E_A remains relatively stable at ~12 μC/cm^2 and ~60 kV/cm, respectively, as shown in Figure 6b. While the P_{max} increases significantly and the E_F decreases as the temperature rises, the increase in P_{max} is due to the enhanced mobility of the domain walls at higher temperatures, while the decrease of E_F is possibly related to a reduction in the free-energy barrier between the FE and AFE phases [29,30]. This is attributed to the increased ability of domain-wall motion at elevated temperatures [31,32]. As a result, the W_{rec} and η increase obviously from 1.34 J/cm^3 to 2.09 J/cm^3 and from 30.5% to 32.9%, respectively, as show in Figure 6c. Figure 6d demonstrates the frequency-dependent behavior of *P-E* loops at RT. Figure 6e,f show the small variations of E_F, E_A, P_{max}, P_r, $W_{rec,}$ and η under various frequencies. P_{max} possesses a linear decreasing dependence on the logarithm of frequency, resulting in a decrease in its energy-storage density. Additionally, it can be observed that E_F decreases as frequency increases; on the contrary, E_A increases. This leads to a decrease in hysteresis ΔE (E_F-E_A) as frequency increases, resulting in an increase in η. However, the variation is less than 5%, indicating good stability. Thus, both W_{rec} and η also exhibit good stability with frequency in the range of (1–300 Hz).

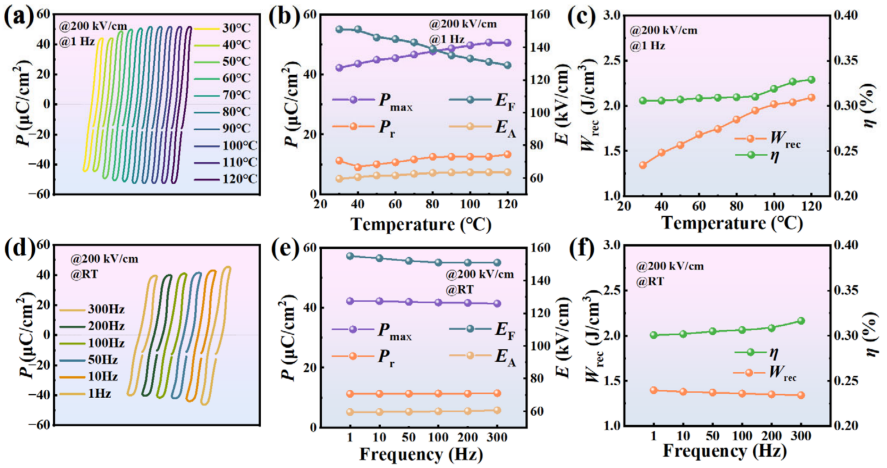


Figure 6. (**a**) Temperature dependence of *P-E* loops in the range of RT-120 °C, and the corresponding (**b**) E_F, E_A, P_{max}, P_r and (**c**) W_{rec} and η for [001]-oriented AN single crystal. (**d**) Frequency dependence of *P-E* loops under various frequencies, and the corresponding (**e**) E_F, E_A, P_{max}, P_r and (**f**) W_{rec} and η for [001]-oriented AN single crystal.

Ultimately, a high-quality AN single crystal was grown using AgCl as flux. The fundamental properties for [001]-oriented AN single crystals were systematically investigated in detail for the first time. In order to make a clearer understanding of the as-grown AN single crystal in this work, some other previously reported AN single crystal and AN ceramic are listed in Table 2. The AN single crystal exhibits higher phase-transition temperatures, higher dielectric constant, lower dielectric loss, and better optical transmittance compared with ceramics. Furthermore, this work also shows a more comprehensive understanding of the structure and other electrical properties when compared with the previously reported AN single crystals.

Table 2. Comparison of AN single crystal and ceramic data.

		The [001]-Oriented AN Single Crystal AN Single Crystal	AN Ceramic	Previous Research for AN Single Crystal
Phase transition temperature (°C)	M1-M2	80	67	~80
	M2-M3	295	268	~280
	M3-O	412	354	~390 [33]
Dielectric constant (100 kHz)		400–2000	200–1000	300–2000 [34]
Dielectric loss (100 kHz)		0–0.4	0–1.0	0–0.4
Electric domain	Size (μm)	10–20		
	Domain Wall (°)	90		90 [35]
Infrared transmittance (1000–4000 cm^{-1})	1000–1500 (%)	56–62	40–59	
	1500–4000 (%)	42–56	20–40	
	P_{max} (μC/cm^2)	42.2	42.1	22 (E//[110]) [36]
Electrical properties (200 kV/cm)	P_r (μC/cm^2)	11.3	7.8	
	W_{rec} (J/cm^3)	1.34	1.98	
	η (%)	30	29.80	
	E_A (kV/cm)	59		
	E_F (kV/cm)	151		

To minimize the influence of other factors, the raw materials of AN ceramic for comparison were consistently with AN single crystal and sintered at 1080 °C for 6 h under an oxygen atmosphere.

4. Conclusions

In this study, we successfully grew AN single crystals with regular geometry using the flux method. The dimensions of the crystals reached up to 5 × 5 × 3 mm³, which met the requirements for investigating the intrinsic structure and its exceptional electrical properties. It was found that the AN single crystal has more obvious transmission characteristics for infrared light. The [001]-oriented AN single crystal displayed a dual-domain, stripe-like antiferroelectric structure with 90° domain walls; approximately temperature-dependent dielectric spectra and high-temperature XRD results showed that it exhibited a similar phase transition sequence to AN ceramic and possessed a higher dielectric constant but a lower loss, which indicated higher electric resistivity. It also had W_{rec} and η comparable to ceramic. Moreover, it showed a typical double *P-E* loop associating antiferroelectric behavior and exhibited good stability within the range of RT-120 °C and 1–300 Hz. These findings could provide valuable support and optimization possibilities for future research on AN-based material.

Author Contributions: Conceptualization, D.Z. and N.L.; methodology, D.Z. and Z.C.; validation, N.L.; formal analysis, D.Z. and N.L.; investigation, D.Z., Z.C., B.L., S.F. and N.L.; resources, D.Z. and N.L.; data curation, D.Z. and N.L.; writing—original draft preparation, D.Z. and N.L.; writing—review and editing, D.Z. and N.L.; visualization, D.Z. and N.L.; supervision, N.L.; project administration, N.L.; funding acquisition N.L. All authors have read and agreed to the published version of the manuscript.

Funding: This work was financially supported by the National Natural Science Foundation of China (Grant No. 52072080) and Guangxi Natural Science Fund for Distinguished Young Scholars (Grant No. 2022GXNSFFA035034).

Data Availability Statement: The data presented in this study are available on request from the corresponding author.

Acknowledgments: We would like to thank Xiyong Chen from the School of Resources, Environment and Materials of Guangxi University for his help with the instrumentation of the Polarized Light Microscope.

Conflicts of Interest: The authors declare no conflicts of interest.

References

1. Liu, H.; Sun, Z.; Zhang, J.; Luo, H.; Zhang, Q.; Yao, Y.; Deng, S.; Qi, H.; Liu, J.; Gallington, L.C.; et al. Chemical Design of Pb-Free Relaxors for Giant Capacitive Energy Storage. *J. Am. Chem. Soc.* **2023**, *145*, 11764–11772. [CrossRef]
2. Yang, L.; Kong, X.; Li, F.; Hao, H.; Cheng, Z.; Liu, H.; Li, J.-F.; Zhang, S. Perovskite Lead-Free Dielectrics for Energy Storage Applications. *Prog. Mater Sci.* **2019**, *102*, 72–108. [CrossRef]
3. Ma, L.; Che, Z.; Xu, C.; Cen, Z.; Feng, Q.; Chen, X.; Toyohisa, F.; Li, J.-F.; Zhang, S.; Luo, N. High Energy Storage Density and Efficiency in $AgNbO_3$ Based Relaxor Antiferroelectrics with Reduced Silver Content. *J. Eur. Ceram. Soc.* **2023**, *43*, 3228–3235. [CrossRef]
4. Lu, Z.; Bao, W.; Wang, G.; Sun, S.-K.; Li, L.; Li, J.; Yang, H.; Ji, H.; Feteira, A.; Li, D.; et al. Mechanism of Enhanced Energy Storage Density in $AgNbO_3$-Based Lead-Free Antiferroelectrics. *Nano Energy* **2021**, *79*, 105423. [CrossRef]
5. Han, K.; Luo, N.; Mao, S.; Zhuo, F.; Liu, L.; Peng, B.; Chen, X.; Hu, C.; Zhou, H.; Wei, Y. Ultrahigh Energy-Storage Density in A-/B-Site Co-Doped $AgNbO_3$ Lead-Free Antiferroelectric Ceramics: Insight into the Origin of Antiferroelectricity. *J. Mater. Chem. A* **2019**, *7*, 26293–26301. [CrossRef]
6. Luo, N.; Ma, L.; Luo, G.; Xu, C.; Rao, L.; Chen, Z.; Cen, Z.; Feng, Q.; Chen, X.; Toyohisa, F.; et al. Well-Defined Double Hysteresis Loop in $NaNbO_3$ Antiferroelectrics. *Nat. Commun.* **2023**, *14*, 1776. [CrossRef]
7. Fu, D.; Endo, M.; Taniguchi, H.; Taniyama, T.; Itoh, M. $AgNbO_3$: A Lead-Free Material with Large Polarization and Electromechanical Response. *Appl. Phys. Lett.* **2007**, *90*, 252907. [CrossRef]
8. Gao, J.; Li, Q.; Zhang, S.; Li, J.-F. Lead-Free Antiferroelectric $AgNbO_3$: Phase Transitions and Structure Engineering for Dielectric Energy Storage Applications. *J. Appl. Phys.* **2020**, *128*, 070903. [CrossRef]
9. Gao, J.; Zhang, Y.; Zhao, L.; Lee, K.-Y.; Liu, Q.; Studer, A.; Hinterstein, M.; Zhang, S.; Li, J.-F. Enhanced Antiferroelectric Phase Stability in La-Doped $AgNbO_3$: Perspectives from the Microstructure to Energy Storage Properties. *J. Mater. Chem. A* **2019**, *7*, 2225–2232. [CrossRef]
10. Shi, X.; Eckstein, U.; Lang, S.; Cicconi, M.R.; Khansur, N.H. Temperature-Dependent Ferroelastic Behaviour of Antiferroelectric $AgNbO_3$. *Acta Mater.* **2022**, *232*, 117931. [CrossRef]

11. Zhang, Y.; Li, X.; Song, J.; Zhang, S.; Wang, J.; Dai, X.; Liu, B.; Dong, G.; Zhao, L. $AgNbO_3$ Antiferroelectric Film with High Energy Storage Performance. *J. Mater.* **2021**, *7*, 1294–1300. [CrossRef]
12. Yang, D.; Su, M.; Yuan, C.; Wu, J.; Meng, L.; Xu, J.; Lei, W.; Feng, Q.; Zhu, B.; Zhou, C.; et al. $AgNbO_3$-Based Antiferroelectric Ceramics with Superior Energy Storage Performance via Gd/Ta Substitution at A/B Sites. *Ceram. Int.* **2023**, *49*, 18143–18152. [CrossRef]
13. Zhou, Y.; Gao, S.; Huang, J.; Shen, M.; Jiang, S.; He, Y.; Zhang, Q. Realizing Simultaneously Excellent Energy Storage and Discharge Properties in $AgNbO_3$ Based Antiferroelectric Ceramics via La^{3+} and Ta^{5+} Co-Substitution Strategy. *J. Mater.* **2023**, *9*, 410–421. [CrossRef]
14. Zhou, Y.; Tang, Z.; Bai, Y.; Guo, F.; Chen, J. Surface Plasma Treatment Boosting Antiferroelectricity and Energy Storage Performance of $AgNbO_3$ Film. *J. Eur. Ceram. Soc.* **2023**, *44*, 2923–2933. [CrossRef]
15. Zhou, J.; Du, J.; Chen, L.; Li, Y.; Xu, L.; Zhao, Q.; Yang, H.; Ding, J.; Sun, Z.; Hao, X.; et al. Enhanced the Energy Storage Performance in $AgNbO_3$-based Antiferroelectric Ceramics via Manipulation of Oxygen Vacancy. *J. Eur. Ceram. Soc.* **2023**, *43*, 6059–6068. [CrossRef]
16. Luo, N.; Han, K.; Cabral, M.J.; Liao, X.; Zhang, S.; Liao, C.; Zhang, G.; Chen, X.; Feng, Q.; Li, J.-F.; et al. Constructing Phase Boundary in $AgNbO_3$ Antiferroelectrics: Pathway Simultaneously Achieving High Energy Density and Efficiency. *Nat. Commun.* **2020**, *11*, 4824. [CrossRef]
17. Gao, S.; Huang, Y.; Jiang, Y.; Shen, M.; Huang, H.; Jiang, S.; He, Y.; Zhang, Q. Ultrahigh Energy Density and Excellent Discharge Properties in Ce^{4+} and Ta^{5+} Co-Modified $AgNbO_3$ Relaxor Antiferroelectric Ceramics via Multiple Design Strategies. *Acta Mater.* **2023**, *246*, 118730. [CrossRef]
18. Chien, R.R.; Tu, C.-S.; Schmidt, V.H.; Wang, F.-T. Electric-Field-Induced and Temperature-Induced Phase Transitions in High-Strain Ferroelectric Pb $(Mg_{1/3}Nb_{2/3})_{0.67}$ $Ti_{0.33}O_3$ Single Crystal. *J. Phys. Condens. Matter* **2006**, *18*, 8337–8344. [CrossRef]
19. Bokov, A.A.; Long, X.; Ye, Z.-G. Optically Isotropic and Monoclinic Ferroelectric Phases in Pb $(Zr_{1-x}Ti_x)$ O_3 (PZT) Single Crystals near Morphotropic Phase Boundary. *Phys. Rev. B* **2010**, *81*, 172103. [CrossRef]
20. Yashima, M.; Matsuyama, S.; Sano, R.; Itoh, M.; Tsuda, K.; Fu, D. Structure of Ferroelectric Silver Niobate $AgNbO_3$. *Chem. Mater.* **2011**, *23*, 1643–1645. [CrossRef]
21. Ratuszna, A.; Pawluk, J.; Kania, A. Temperature Evolution of the Crystal Structure of $AgNbO_3$. *Phase Transit.* **2003**, *76*, 611–620. [CrossRef]
22. Khor, C.M.; Khan, M.M.; Khan, M.Y.; Khan, A.; Harunsani, M.H. Zr-Doped $AgNbO_3$ with Enhanced Visible Light-Induced Photocatalytic Performance. *Results Chem.* **2023**, *5*, 100891. [CrossRef]
23. Khor, C.M.; Khan, M.M.; Khan, A.; Khan, M.Y.; Harunsani, M.H. La-Substituted $AgNbO_3$ for Photocatalytic Degradation of Rhodamine B and Methylene Blue Dyes. *React. Kinet. Mech. Catal.* **2022**, *135*, 1687–1701. [CrossRef]
24. Ai, J.; Chen, X.; Luo, L.; Zheng, R.; Yu, L. Novel Transparent Eu and Hf Co-Doped $AgNbO_3$ Antiferroelectric Ceramic with High-Quality Energy-Storage Performance. *Ceram. Int.* **2022**, *48*, 23630–23637. [CrossRef]
25. Palaimienė, E.; Macutkevič, J.; Banys, J.; Gruszka, I.; Kania, A. Broadband and Infrared Spectroscopy of $Ag_{0.98}Li_{0.02}NbO_3$ Ceramics. *Lith. J. Phys.* **2020**, *60*, 247–252. [CrossRef]
26. Fousek, J.; Janovec, V. The Orientation of Domain Walls in Twinned Ferroelectric Crystals. *J. Appl. Phys.* **1969**, *40*, 135–142. [CrossRef]
27. Zheng, L.; Li, S.; Sang, S.; Wang, J.; Huo, X.; Wang, R.; Yuan, Z.; Cao, W. Complete Set of Material Constants of Single Domain (K, Na) (Nb, Ta) O_3 Single Crystal and Their Orientation Dependence. *Appl. Phys. Lett.* **2014**, *105*, 212902. [CrossRef] [PubMed]
28. Yan, Z.; Zhang, D.; Zhou, X.; Zhang, M.; Zhang, L.; Zhang, H.; Xue, G.; Abrahams, I.; Yan, H. Investigation of Transitions between the M-Phases in $AgNbO_3$ Based Ceramics. *J. Mater. Chem. A* **2021**, *9*, 3520–3529. [CrossRef]
29. Hafid, M.; Kugel, G.E.; Kania, A.; Roleder, K.; Fontana, M.D. Study of the Phase Transition Sequence of Mixed Silver Tantalate-Niobate $(AgTa_{1-x}Nb_xO_3)$ by Inelastic Light Scattering. *J. Phys. Condens. Matter* **1992**, *4*, 2333–2345. [CrossRef]
30. Zhuo, F.; Li, Q.; Zhou, Y.; Ji, Y.; Yan, Q.; Zhang, Y.; Xi, X.; Chu, X.; Cao, W. Large Field-Induced Strain, Giant Strain Memory Effect, and High Thermal Stability Energy Storage in (Pb, La) (Zr, Sn, Ti) O_3 Antiferroelectric Single Crystal. *Acta Mater.* **2018**, *148*, 28–37. [CrossRef]
31. Zhao, L.; Liu, Q.; Zhang, S.; Li, J.-F. Lead-Free $AgNbO_3$ Anti-Ferroelectric Ceramics with an Enhanced Energy Storage Performance Using MnO_2 Modification. *J. Mater. Chem. C* **2016**, *4*, 8380–8384. [CrossRef]
32. Cai, K.; Yan, X.; Deng, P.; Jin, L.; Bai, Y.; Zeng, F.; Guo, D. Phase Coexistence and Evolution in Sol-Gel Derived BY-PT-PZ Ceramics with Significantly Enhanced Piezoelectricity and High Temperature Stability. *J. Mater.* **2019**, *5*, 394–403. [CrossRef]
33. Wada, S.; Uraki, S.; Kakemoto, H.; Tsurumi, T. Growth of Silver Niobate Single Crystals and Their Dielectric Properties. *J. Ceram. Soc. Jpn.* **2004**, *112*, S780–S784.
34. Kania, A. Anisotropic Dielectric Properties of $AgNbO_3$ Single Crystals. *Ferroelectrics* **2010**, *404*, 152–156. [CrossRef]
35. Zhao, W.; Fu, Z.; Deng, J.; Li, S.; Han, Y.; Li, M.-R.; Wang, X.; Hong, J. Observation of Ferroelastic and Ferroelectric Domains in $AgNbO_3$ Single Crystal. *Chin. Phys. Lett.* **2021**, *38*, 037701. [CrossRef]
36. Kitanaka, Y.; Egawa, T.; Noguchi, Y.; Miyayama, M. Enhanced Polarization Properties of Ferrielectric $AgNbO_3$ Single Crystals Grown by Czochralski Method under High-Pressure Oxygen Atmosphere. *Jpn. J. Appl. Phys.* **2016**, *55*, 10TB03. [CrossRef]

Disclaimer/Publisher's Note: The statements, opinions and data contained in all publications are solely those of the individual author(s) and contributor(s) and not of MDPI and/or the editor(s). MDPI and/or the editor(s) disclaim responsibility for any injury to people or property resulting from any ideas, methods, instructions or products referred to in the content.